Fabrication of Highly Porous Platinum by Cyclic Electrodeposition of PtCu Alloys: How do Process Parameters Affect Morphology?

Arne Kloke,[a] Christian Köhler,[a] Anna Dryzga,[b] Ramona Gerwig,[c] Katrin Schumann,[a,d] Martin Ade,[e] Roland Zengerle,[a,f] and Sven Kerzenmacher[a,z]

[a]*IMTEK - Department of Microsystems Engineering, University of Freiburg, 79110 Freiburg, Germany*
[b]*HSG-IMIT - Institut für Mikro- und Informationstechnik, 79110 Freiburg, Germany*
[c]*Natural and Medical Sciences Institute at the University of Tübingen, 72770 Reutlingen, Germany*
[d]*Karlsruhe Institute of Technology (KIT), 76021 Karlsruhe, Germany*
[e]*Institute for Inorganic and Analytical Chemistry, University of Freiburg, 79104 Freiburg, Germany*
[f]*BIOSS, Centre for Biological Signalling Studies, University of Freiburg, 79110 Freiburg, Germany*

In this work we analyze the influence of process parameters on the morphology of highly porous platinum electrodes, fabricated by co-deposition of platinum-copper alloy and subsequent selective dissolution of the less noble copper during multiple cyclic voltammetry scans. Thereto the Cu^{2+} concentration in the deposition electrolyte, the negative scan limit, and the scan rate were varied. Corresponding electrodes were characterized by their surface texture (scanning electron microscopy, X-ray diffractometry), specific surface area, and elemental compositions (X-ray photoelectron spectroscopy and energy dispersive X-ray spectroscopy). Under conditions enforcing precursor depletion a sphere-dominated structure is observed, whereas oppositional configurations lead to smoother, mud-crack pattern like structures. Electrodes of high specific surface area are obtained particularly when high copper ion concentrations (100 mmol l^{-1} $CuSO_4$, roughness factor 3740 ± 270), high negative scan limits (−0.800 V vs. SCE, roughness factor 3790 ± 370) and low scan speeds (1 mV s^{-1}, roughness factor 3930 ± 370) compared to standard parameters (20 mmol l^{-1} $CuSO_4$, −0.600 V vs. SCE negative scan limit, 1 mV s^{-1}, roughness factor 3040 ± 300) were applied during fabrication. Since the fabrication of these highly rough electrodes requires the deposition of high amounts of platinum (10–20 mg per cm^2 footprint area) it is mainly relevant to applications such as neurostimulation electrodes or implantable glucose fuel cells in which platinum costs are less relevant than electrode properties and functionality.
© 2013 The Electrochemical Society. [DOI: 10.1149/2.001304jes] All rights reserved.

Catalytically active platinum structures[1,2] are of great importance for a wide range of applications. Examples are energy conversion in e.g. fuel cells,[3] chemical engineering of organic reactions,[4,5] sensors for e.g. the enzyme-free detection of glucose,[6–8] and biomedical devices such as neurostimulation electrodes.[9,10] In particular for small scale applications the direct electrodeposition of porous platinum structures is a preferred approach due to its high precision, good controllability, and compatibility with microfabrication techniques.[1]

One focus of research in the field of electrodeposited platinum structures is the maximization of specific surface area to increase the reaction rate of kinetically controlled reactions,[6–8,11] or to decrease e.g. the impedance of the implant-tissue interface in *neural stimulation and recording electrodes* which improves the signal to noise ratio.[9,10] Another aspect is the investigation of catalytic effects that depend on the nanoscopic texture or surface orientation of e.g. platinum particles and crystallites.[12–14] For instance Tian et al. observed a two times higher oxidation current density (per electrochemically active area) for formic acid oxidation when using nanocrystals with high-index facets compared to nanoparticles of similar diameter, but with non-defined low-index facets.[15] On the macroscale, the morphology of porous platinum structures has a distinct influence on the accessibility of catalytically active sites, which can help to improve selectivity or enhance mass transport rates. Examples are *non-enzymatic glucose sensors* in which the sensitivity toward interfering substances is reduced by tuning the mass-transport characteristics of the electrode.[6–8] Similarly, accessibility can be used to control the selectivity of platinum electrodes for either oxygen reduction or glucose oxidation in *implantable glucose fuel cells* which have to be operated in a mixture containing both reactants.[11]

In a previous publication we introduced the cyclic electrodeposition of PtCu alloy as a facile method for the fabrication of porous platinum electrodes with controllable specific surface area.[11] This process is based on the alternation of co-deposition of PtCu alloy and subsequent selective dissolution of Cu (dealloying) during multiple cyclic voltammetry (CV) scans in a deposition electrolyte containing H_2PtCl_6 and $CuSO_4$ (20 mmol l^{-1} each) in sulfuric acid (0.5 mol l^{-1}). Electrodes fabricated with 500 deposition cycles (50 mV s^{-1},

1.400 to −0.600 V vs. SCE) showed a cauliflower-like microstructure and roughness factors of up to 3070 ± 300 (RF, ratio between electrochemically active area and geometric footprint).

In the present work, we now investigate how the variation of Cu^{2+} concentration, negative scan limit and scan rate can be used to control the morphology (surface texture and specific surface area) of such electrodeposited porous platinum structures. Further nanoscopic properties such as elemental composition and crystallite size were analyzed by means of EDX (energy dispersive X-ray spectroscopy), XPS (X-ray photoelectron spectroscopy) and XRD (X-ray diffraction).

Materials and Methods

Substrate preparation.— Substrates for electrode fabrication were prepared as described elsewhere.[11] In short, substrate chips (1.6 × 1.7 cm^2) with 1 cm^2 active area were fabricated by evaporation of 50 nm titanium followed by 250 nm platinum onto silicon wafers (⟨100⟩ orientation, 525 μm thickness, n^+ type doped) through a photolithography template and subsequent wafer cutting. Before use, all samples were cleaned in an ultrasonic bath (acetone, isopropyl alcohol, deionized water, 2 min each), weighed (with ± 3 μg accuracy; SC 2, Sartorius, Göttingen, Germany) and inserted in a sample holder exposing only the active area and enabling the connection of separate platinum wires for current and potential (50 μm diameter, Chempur, Karlsruhe). Subsequently, cyclic voltammetry (CV) scans (10 cycles, 50 mV s^{-1}, 1.400 to −0.400 V vs. saturated calomel electrode (SCE, KE11, Sensortechnik Meinsberg, Ziegra-Knobelsdorf, Germany), no agitation, room temperature) were performed in sulfuric acid (0.5 mol l^{-1}, Merck, Darmstadt, Germany) to further clean the substrate surface.

Electrode fabrication.— Porous platinum electrodes were fabricated at room temperature by performing CV scans in 50 mL deposition electrolyte prepared from sulfuric acid (0.5 mol l^{-1}) and the precursor salts hexachloroplatinic acid (H_2PtCl_6, 20 mmol l^{-1}, Chempur, Karlsruhe, Germany) and copper sulfate ($CuSO_4$, Merck Chemicals, Darmstadt, Germany) in the absence of agitation. In our previous publication we used 500 CV scans between 1.400 and −0.600 V vs. SCE at a scan rate of 50 mV s^{-1} in an electrolyte with an addition of

[z]E-mail: kerzenma@imtek.de

20 mmol l^{-1} copper sulfate as a standard parameter set for highly porous electrodes.[11] In the present study, we varied the concentration of copper sulfate (0 to 100 mmol l^{-1}), negative scan limit (−0.800 to −0.200 V vs. SCE), and scan rate (1 to 250 mV s^{-1}) while keeping the other parameters unchanged compared to the standard parameter set. For different scan rates, also the number of deposition cycles was adjusted to keep the same deposition and overall process times. Therefore we for instance performed 2500 deposition cycles instead of 500, when increasing the scan speed from 50 to 250 mV s^{-1}.

Electrode cleaning and characterization.— Subsequent to fabrication the electrodes were cleaned by CV scans in sulfuric acid as described above for substrate cleaning. Additional CV scans were performed for determination of the roughness factor as quantitative measure of the specific surface area. Here slow scan rates (≤ 2 mV s^{-1}) and adjusted negative scan limits were applied to determine the desorption charges related to underpotential deposition of a complete hydrogen monolayer as precisely as possible.[16]

A Solatron 1470E Cell Test System (Ametek, Farnborough, UK) was used as potentiostat for fabrication and electrochemical characterization in combination with a roughened platinum wire (0.4 μm diameter, Chempur, Karlsruhe, Germany) serving as counter electrode. Before and after fabrication, electrode substrates were weighed to determine the total deposited mass, and by consideration of the Cu-content measured by EDX (energy dispersive X-ray spectroscopy) also the deposited platinum mass $m_{dep,Pt}$. As a measure for platinum utilization we calculated the ratio of surface atoms r_{sa} by comparison of the number of surface platinum atoms N_{sa} and the total number of platinum atoms N_{total} which can be derived from the roughness factor RF and deposited platinum mass $m_{dep,Pt}$. (deposited mass is corrected by Cu-content measured via EDX) according to:

$$r_{sa} = \frac{N_{sa}}{N_{total}} = \frac{\rho_{sa} RF A_{el}}{m_{dep,Pt}/m_{pt}} \qquad [1]$$

Here ρ_{sa} is the average density of surface platinum atoms (1.31 10^{15} atoms cm^{-2},[16]), A_{el} the footprint size of the electrode and m_{Pt} the mass of a single platinum atom (3.24 10^{-19} mg).

Scanning electron microscopy (SEM) images were taken with a Zeiss Supra 60 VP (working distance 3 mm, 5 kV acceleration voltage). EDX-spectra were recorded for an analysis area of 2×2 mm^2 with a Six X-ray instrument (Thermo Scientific, Wilmington MA, USA). XPS-spectra (X-ray photoelectron spectroscopy) were recorded by ten sweeps from 1360 to 0 eV over an analysis area of 1.4 $\times$ 1.4 mm^2 using the high resolution XPS-instrument PHI Quantera SXM (X-ray source: Al K α, E = 1486.6 eV, Physical Electronics Inc., Chanhassen MN, USA).

X-ray diffraction (XRD) data were collected using a Siemens D5000 instrument with Cu Kα radiation, a secondary monochromator (LiF) and a scintillation detector. Measurements were performed in grazing incidence diffraction (GID) geometry in order to avoid penetration of the primary beam to the substrate. The incidence angle to the sample surface was set to 1°, whereas the diffraction angle (2 theta) was scanned from 10° to 60° (0.04° step size, 10 s each) during data acquisition. Lattice constants a were derived from positions of (110) and (200) reflexes using the quadratic equation for face centered cubic (fcc) crystals[17,18]

$$a = \lambda \frac{\sqrt{(h^2 + k^2 + l^2)}}{2 sin \Theta} \qquad [2]$$

Here h, k, l stand for the Miller indexes and θ for the Bragg angle at which the reflex is observed, λ is the X-ray wavelength (1.541874 Å for this instrument). Crystallite sizes d were derived from the full width at half maximum $\Delta(2\theta)$ observed for the different reflexes (hkl) given in radians using the Scherrer equation:[19,20]

$$d = \frac{K \lambda}{\Delta(2\Theta) cos \Theta} \qquad [3]$$

Here K is the shape factor, λ is the X-ray wavelength, θ is the Bragg angle position of the reflex.

Results and Discussion: Individual effects of process parameters

The deposition process.— Figure 1A shows first cycles of CV scans recorded in electrolytes of different CuSO$_4$ concentration (0 to 30 mmol l^{-1}). In the cathodic scan platinum deposition occurs for potentials more negative than 0.50 V vs. SCE. The presence of copper in the electrolyte leads to additional currents at potentials more negative than 0.50 V vs. SCE. In the range of 0.50 to 0.25 V vs. SCE these currents are related to underpotential deposition (UPD) of copper, whereas at electrode potentials more negative than 0.25 V vs. SCE bulk deposition of copper occurs.[21,22] Thus a co-deposition of platinum and copper takes place during the cathodic scan for potentials more negative than 0.50 V vs. SCE. In literature, electrochemical fabrication of co-deposits has been shown by the application of both underpotential deposition (UPD),[22] and bulk-deposition.[23] Since UPD is thermodynamically limited to the deposition of up to one monolayer,[21] increases in current density caused by the co-deposition of copper are
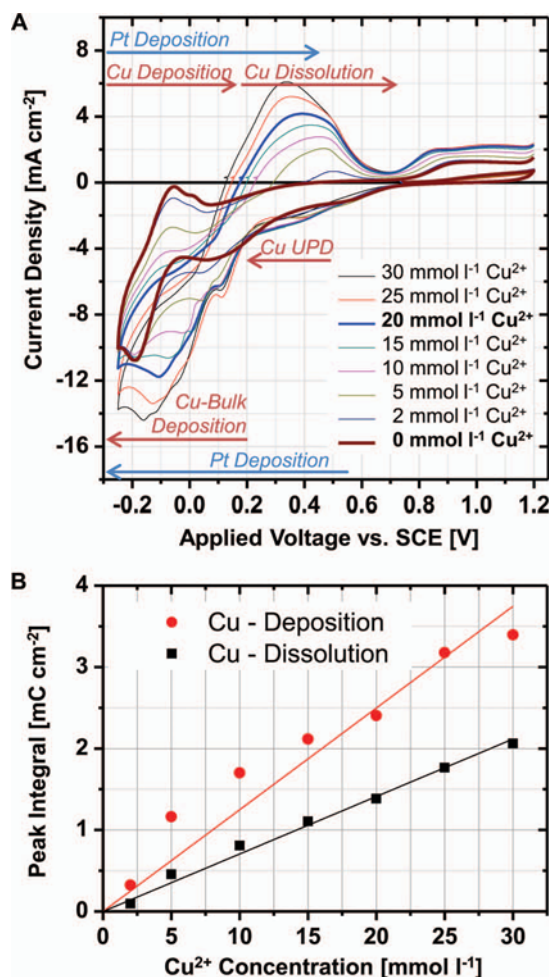
Figure 1. Comparison of first deposition cycles at various concentrations of Cu^{2+}. A) CV scans (50 mV s^{-1}, 1.200 to −0.250 V vs. SCE) recorded in 0.5 mol l^{-1} H$_2$SO$_4$ with addition of H$_2$PtCl$_6$ (20 mmol l^{-1}) and CuSO$_4$ at various concentrations (0 to 30 mmol l^{-1}). As negative scan limit −0.250 V vs. SCE was chosen to exclude superposition of the deposition-dissolution signals by hydrogen generation and thus allow for process identification. A figure showing first deposition cycles recorded with negative scan limit −0.600 V vs. SCE is given in the supplementary (Figure S1). B) Relationship between charges associated with copper deposition and dissolution and Cu^{2+} concentration in the electrolyte (see supplementary for details, Figure S2).

significantly lower in potential ranges where UPD is taking place compared to when bulk deposition occurs (see Figure 1A). Therefore, most of the deposited copper is related to the bulk deposition process. Within the anodic scan, the presence of copper leads to the appearance of an additional peak approximately at a potential between 0.1 and 0.7 V vs. SCE indicating copper dissolution. For both processes, copper co-deposition and copper dissolution higher currents are observed for increasing copper concentrations.

The relationship between Cu^{2+}-concentration and the charges associated with copper deposition and dissolution are shown in Figure 1B, respectively. Charges were obtained by integration of the CV scans within the potential ranges corresponding to the deposition and dissolution of copper after subtracting CV scans recorded in the copper-free electrolyte (see supplementary for details, Figure S2). The linear dependency of charge on Cu^{2+}-concentration indicates mass transport limitation for both processes. Furthermore, lower charges are obtained for copper dissolution compared to deposition, indicating incomplete dealloying of copper from the deposited alloy. This is in agreement with a residual copper content of 3–10 atom% found in the final electrode structure by XPS analysis.[11]

To fabricate highly porous platinum electrodes, the process shown in Figure 1A is repeated by performing multiple CV scans and thus deposition cycles. This way the structure generated during the previous deposition cycle serves as an already high surface area substrate during the subsequent deposition cycle, enabling a continuous growth of the electrode surface. When these CV scans (50 mV s^{-1}, 1.400 and −0.600 V vs. SCE) are performed in sulfuric acid containing 20 mmol l^{-1} of each platinum and copper the increase in surface roughness saturates in the range of 500 deposition cycles at roughness factor of 3070 ± 300, as shown in our previous publication.[11]

In the following, these established standard parameters are now used as a starting point to investigate the effect of Cu^{2+} concentration, negative scan limit, and scan rate on electrode morphology.
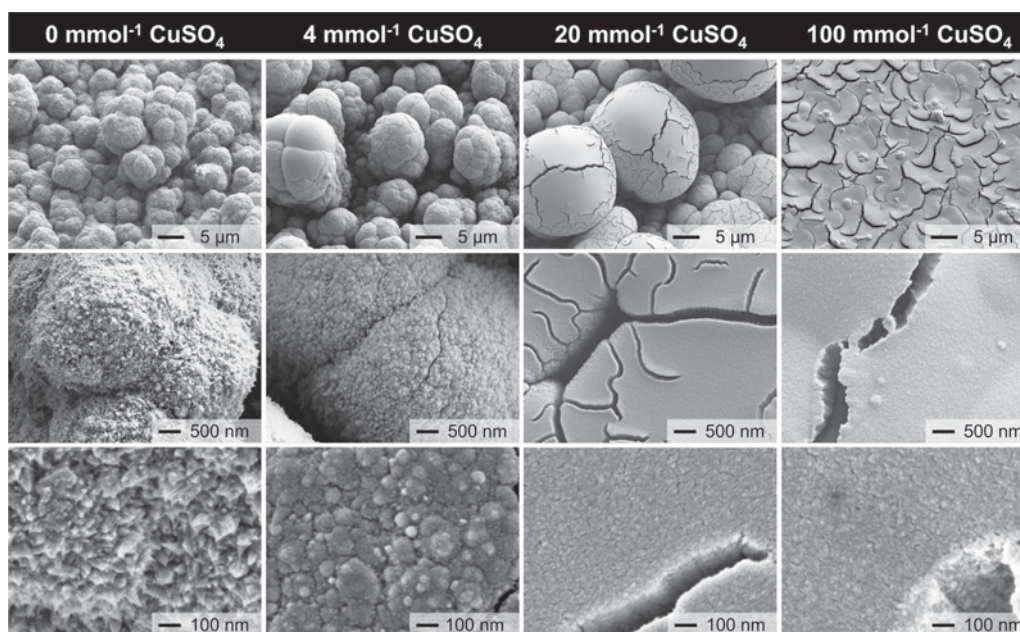
Effects of the concentration of Cu^{2+} in the deposition electrolyte.— In Figure 2 SEM micrographs of electrodes fabricated with standard parameters (500 cycles at 50 mV s^{-1} between 1.400 and −0.600 V vs. SCE, 20 mmol l^{-1} of each platinum and copper) are compared to electrodes fabricated in deposition electrolytes of different Cu^{2+} con-

centrations varied from 0 to 100 mmol l^{-1}. Here a clear influence of copper concentration on the surface texture is observed: at low copper concentrations (0 to 20 mmol l^{-1} Cu^{2+}) cauliflower-like structures are obtained, and the size of the cauliflower spheres increases with copper concentration. At 20 mmol l^{-1} Cu^{2+} some smaller spheres have already merged into a flat layer with individual freestanding bigger spheres situated on top. At the highest investigated copper concentration of 100 mmol l^{-1} no individual cauliflower-spheres are observed and an almost flat structure with fractures (mud-crack pattern) is obtained. Also at higher magnifications a significant change in morphology is apparent: without copper in the electrolyte thorn-like dendritic surface structures at a length-scale of 50–100 nm are obtained, whereas the presence of copper leads to less dendritic structures.

The evaluation of specific surface area (expressed as roughness factor, see Table I) reveals an increase in roughness factor with increasing Cu^{2+} concentration. This result is contradictory to the smoother surface texture observed from electron micrographs. This indicates that in particular for the electrodes fabricated with 20 or 100 mmol l^{-1} $CuSO_4$ most of the specific surface area is actually present in a system of micro- and nanoporous fractures below the "smooth" top-layer.

Overall, the roughness factors of RF = 3000 and higher achieved with most of the here discussed parameter sets exceeds the typical range of electrodeposited platinum, which is about up to RF = 1000.[1] A limitation of the here presented method is the requirement of high platinum masses in electrode fabrication (12.1 to 20.8 mg per cm^2 of electrode footprint). Nevertheless the platinum utilization of our method, expressed as active surface area per deposited platinum mass amounts to 83 to 228 cm^2 mg^{-1} which is comparable to other methods. For instance Liu et al. reported up to 322 cm^2 mg^{-1} at RF = 720 for their electrochemical alloying-dealloying process;[23] Choi et al. reported up to 470 cm^2 mg^{-1} at RF = 29 for a fabrication process using templates.[24] For dealloyed Pt-Cu nanoparticles which in contrast to electrodeposition require additional immobilization steps, significantly higher platinum utilization of up to 885 cm^{2}mg^{-1} has been reported.[25]

From comparison of the deposited mass of platinum among the different parameter sets shown in Table I it can be seen that the presence of Cu^{2+} in the deposition electrolyte effectively doubles

Figure 2. SEM images of electrode morphologies obtained from deposition at standard parameters except variation of the concentration of Cu^{2+} in the deposition electrolyte. Upper row shows electron micrographs taken at 6000 × and an angle of 30°. Middle and lower row shows top views taken at 50000 × and 250000 ×, respectively.

Table I. Electrode properties resulting from variation of copper concentration in the deposition electrolyte.

Concentration of Cu^{2+}	No copper	4 mmol l^{-1}	20 mmol l^{-1} (standard)	100 mmol l^{-1}
Roughness factor [*]	1010 ± 240	2800 ± 130	3040 ± 300	3740 ± 270
Deposited Pt-mass [mg cm^{-2}] [*]	12.1 ± 1.4	20.8 ± 1.8	20.0 ± 2.1	19.0 ± 1.9
Surface area per deposited Pt-mass [cm^2 mg^{-1}]	83 ± 22	150 ± 15	176 ± 25	228 ± 28
Proportion of surface platinum atoms [%] [*]	3.5 ± 0.9	6.4 ± 0.6	7.5 ± 1.1	9.7 ± 1.2
Cu content (EDX) [at-%] [**]	0	10 ± 1	14 ± 1	13 ± 1
Cu content (XPS) [at-%] [**]	0	3 ± 1	6 ± 3	4 ± 1
Lattice constant [Å] [***]	3.91 ± 0.01	3.88 ± 0.01	3.88 ± 0.01	3.88 ± 0.01
Crystallite size [nm] [***]	13 ± 2	7 ± 1	8 ± 1	13 ± 2

[*]Mean value ± standard deviation of 4–7 samples.
[**]Mean value ± standard deviation of 2–3 samples.
[***]One sample of was analyzed (same as shown in Figure 2), mean value ± deviation from mean value were calculated from (110) and (200) reflexes.

the amount of platinum deposited per geometric electrode area. This effect is independent of the actual concentration of Cu^{2+}-ions in the electrolyte, whereas the underlying mechanism is not yet understood. Platinum utilization, indicated by the proportion of surface platinum atoms, increases with increasing copper concentration. We assume this to be an effect of the higher copper content in the co-deposited alloy which facilitates pore generation during dealloying.

EDX and XPS analysis reveal residual copper and thus incomplete dealloying for all electrode structures that were fabricated in presence of copper, but no substantial differences in dependence of the actual copper concentration in the deposition electrolyte. Taking into account the lower penetration depth of XPS (few nm) compared to EDX (few 100 nm) the different results observed with the two methods indicate a core-shell like structure with a copper-rich bulk (core) and a copper-poor surface (shell) for all structures, as previously described for electrodes fabricated by our standard parameters and also other PtCu dealloying processes.[11,26,27]

Further analysis of the XPS spectra (see Figure S3–S5) shows no significant differences in composition in dependence of the Cu^{2+} concentration. For all electrodes the platinum peak $4f_{7/2}$ is situated below 72.0 eV clearly indicating metallic platinum (see Figure S4).[28–31] Also copper is most probably present in metallic electron state, since all $2p_{3/2}$ peaks are found in the range of 932.1 to 932.8 eV (see

Figure S5).[28] The presence of Cu^{2+} (like in CuO) can be excluded, since this would lead to strong shake-up satellites in the 2p signal, which is not observed in the recorded spectra.[28,32–34] As the Cu^+-state (e.g. Cu_2O) shows no strong chemical shift of the 2p signal compared to in zero-valent copper,[28] the occurrence of Cu^+ species cannot be excluded from XPS analysis.

XRD analysis indicates a similar nanostructure for all tested electrodes, revealing nanocrystalline Pt and Pt-Cu alloy structures of face center cubic (fcc) lattices with a statistical distribution of the elements, without long range order ([18], see Figure S6 for diffractograms). The lattice constants derived from reflex positions amounts to about 3.88 Å for copper containing electrodes (see Table I) which is between the lattice constants known for the fcc crystals of pure platinum (3.92 Å) and pure copper (3.61 Å).[35] According to Vegard's law (lattice constant shifts linearly with elemental composition,[36]) this indicates a copper content in the range of 10%, which is in agreement with XPS and EDX results. The average crystallite sizes were found to be in the range of 6–15 nm (see Table I), but no trend was observed in dependence on the fabrication parameters.

Effects of negative scan limit.— In Figure 3 SEM micrographs of standard electrodes (500 cycles at 50 mV s^{-1} between 1.400 and
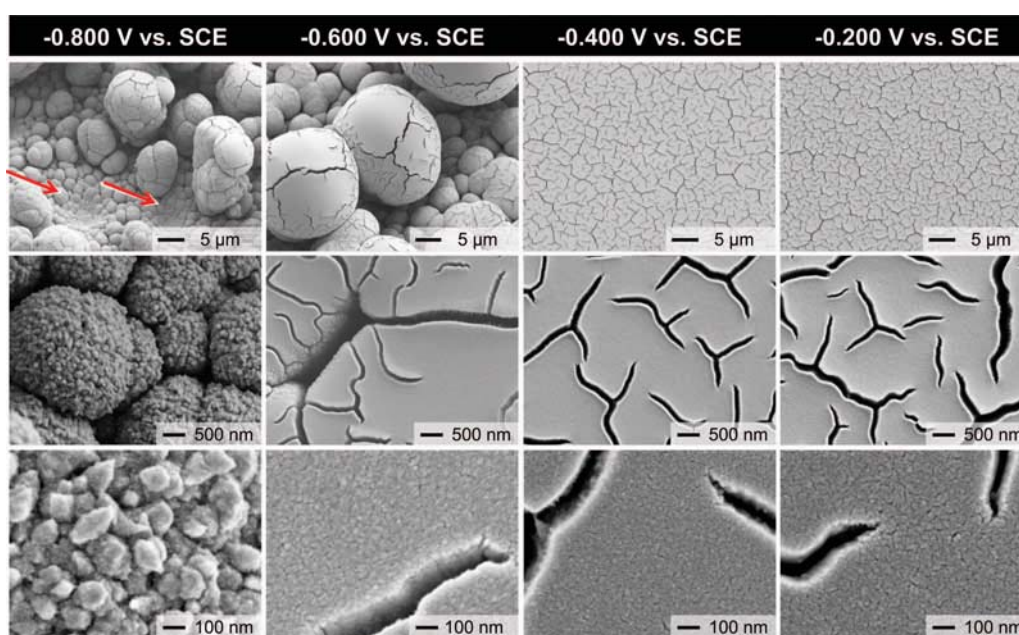
Figure 3. SEM images of electrode morphologies obtained from deposition at standard parameters except different negative scan limits, as indicated in the Figure. Upper row shows electron micrographs taken at 6000 × magnification and an angle of 30°. Middle and lower row shows top views taken at magnifications of 50000 × and 250000 ×, respectively. The red arrows indicate crater-like features which are supposed to result from hydrogen bubble formation during deposition.

Table II. Electrode properties resulting from variation of negative scan limit.

Negative scan limit vs. SCE	−0.200 V	−0.400 V	−0.600 V (standard)	−0.800 V
Roughness factor [*]	1790 ± 110	2710 ± 60	3040 ± 300	3790 ± 370
Deposited Pt-mass [mg cm^{-2}] [*]	6.3 ± 2.9	14.5 ± 0.6	20.0 ± 2.1	23.0 ± 2.9
Surface area per deposited Pt-mass [cm^2 mg^{-1}]	322 ± 152	214 ± 11	176 ± 25	186 ± 30
Proportion of surface platinum atoms [%] [*]	13.7 ± 6.4	9.1 ± 0.5	7.5 ± 1.1	7.9 ± 1.3
Cu content (EDX) [at-%] [**]	12 ± 2	13 ± 2	14 ± 1	11 ± 3
Cu content (XPS) [at-%] [**]	4 ± 2	5 ± 2	6 ± 3	4 ± 1
Lattice constant [Å] [***]	3.90 ± 0.01	3.88 ± 0.01	3.88 ± 0.01	3.88 ± 0.01
Crystallite size [nm] [***]	14 ± 6	8 ± 1	8 ± 1	15 ± 7

[*]Mean value ± standard deviation of 4–7 samples.
[**]Mean value ± standard deviation of 2–3 samples.
[***]Only one sample of was analyzed (same as shown in Figure 3), mean value ± deviation from mean value were calculated from (110) and (200) reflexes. Standard sample (−0.6 V vs. SCE) was analyzed at four different positions, all other samples were measured at a single position.

−0.600 V vs. SCE, 20 mmol l^{-1} of each platinum and copper) are compared to electrodes fabricated with different negative scan limits between −0.800 V and −0.200 V vs. SCE. At low magnification, a transition from cauliflower-like surface texture to a flat surface with mud-crack pattern is observed for less negative values of the negative scan limit, similar as with increasing copper concentration (Figure 2). Furthermore, crater-like areas (see arrow-labels in Figure 3) are obtained when the negative scan limit is set to −0.8 V vs. SCE. We assume that these features are caused by footprints of bubbles resulting from hydrogen generation.[37] On the nanoscale, electrodes fabricated at −0.800 V show a different surface structure with sharp-edged individual particles of approximately 100 nm in diameter. For negative scan limits of −0.600 V, −0.400 V, and −0.200 V less dendritic structures are obtained. Their nanoscale appearance is comparable to the electrodes fabricated with copper contents between 4 and 100 mmol l^{-1} CuSO$_4$ shown in Figure 2.

As a consequence of the extended deposition time per cycle, more platinum is deposited with increasingly negative values of the negative scan limit (see Table II). Consequently, also significantly increased roughness factors are obtained for increasingly negative scan limits.

No significant effects of the negative scan limit are observed on the percentage of surface platinum atoms, residual copper content, crystallite size and lattice constants which were evaluated by EDX, XPS and XRD analysis. The differences in copper contents observed by EDX and XPS analysis again indicate a core-shell structure with a depletion of copper toward the surface.

Effects of scan rate.— In Figure 4 SEM micrographs of electrodes fabricated with standard parameters (1.400 to −0.600 V vs. SCE, 20 mmol l^{-1} CuSO$_4$) are compared to electrodes fabricated at different scan rates between 1 mV s^{-1} and 250 mV s^{-1}. To apply equal deposition times during the fabrication of all electrodes the number of deposition cycles was simultaneously increased as indicated in the headline of Figure 4.

Different to all other parameter sets, electrodes fabricated at 250 mV s^{-1} (2500 deposition cycles) showed to be very fragile exhibiting macroscopic fractures of millimeter size and partial delamination (observed for five out of five samples). Delaminated regions were curved upwards, but still connected to the substrate and other regions of the deposit. This indicates high mechanical tension within
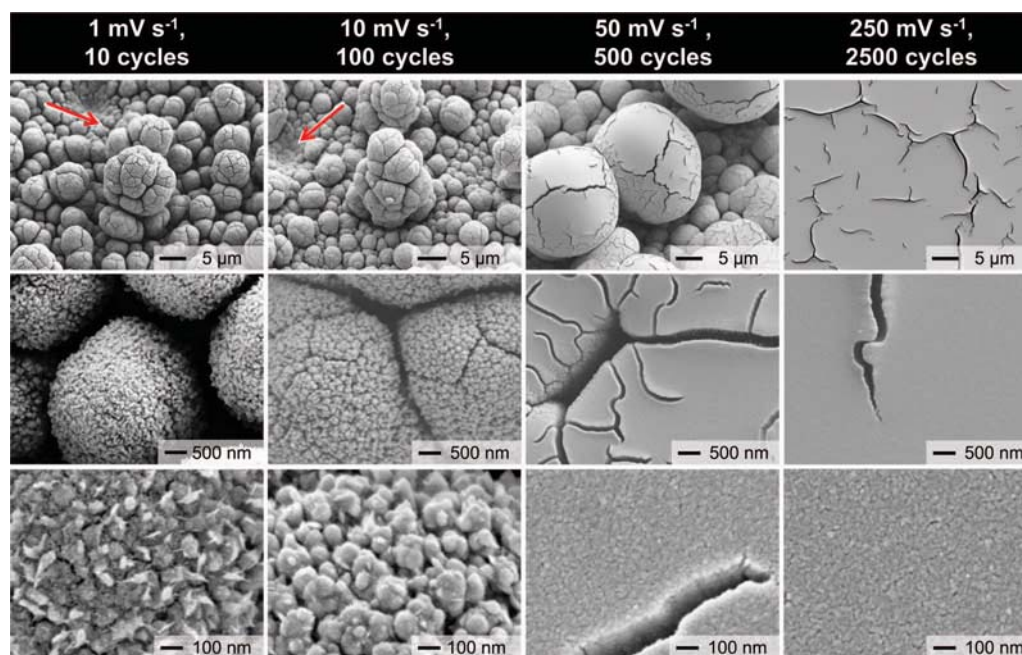
Figure 4. SEM images of electrode morphologies obtained from deposition at standard parameters except different scan rates, as indicated in the Figure. Upper row shows electron micrographs taken at 6000 × magnification and an angle of 30°. Middle and lower row shows top views taken at magnifications of 50000 × and 250000 ×, respectively. The red arrows indicate crater-like features which are supposed to result from hydrogen bubble formation during deposition.

Table III. Electrode properties resulting from variation of scan rate.

Scan rate and adapted number of deposition cycles	1 mV s^{-1}, 10 cycles	10 mV s^{-1}, 100 cycles	50 mV s^{-1}, 500 cycles (standard)	250 mV s^{-1}, 2500 cycles [+]
Roughness factor [*]	3930 ± 370	3490 ± 460	3040 ± 300	(3700 ± 800) [+]
Deposited Pt-mass [mg cm^{-2}] [*]	15.3 ± 3.0	14.5 ± 2.2	20.0 ± 2.1	(12.3 ± 11.4) [+]
Surface area per deposited Pt-mass [cm^2 mg^{-1}]	324 ± 70	277 ± 58	176 ± 25	(335 ± 320) [+]
Proportion of surface platinum atoms [%] [*]	13.7 ± 3.0	11.8 ± 2.5	7.5 ± 1.1	(14.2 ± 13.6) [+]
Cu content (EDX) [at-%] [**]	21 ± 1	13 ± 3	14 ± 1	10 ± 3
Cu content (XPS) [at-%] [**]	9 ± 1	5 ± 1	6 ± 3	6 ± 1
Lattice constant [Å] [***]	3.85 ± 0.01	3.88 ± 0.01	3.88 ± 0.01	3.89 ± 0.01
Crystallite size [nm] [***]	6 ± 2	12 ± 3	8 ± 1	11 ± 1

[*]Mean value $\pm$ standard deviation of 4–7 samples.
[**]Mean value $\pm$ standard deviation of 2–3 samples.
[***]Only one sample of was analyzed (same as shown in Figure 4), mean value $\pm$ deviation from mean value were calculated from (110) and (200) reflexes. Standard sample (-0.6 V vs. SCE) was analyzed at four different positions, all other samples were measured at a single position.
[+]No stable electrode structures were obtained for this parameter. In particular the high surface area is supposed to result from partial detachment or bending of parts of the deposited structure.

the deposit and not adhesion problems as origin of this delamination. To nevertheless generate EDX, XPS, and SEM data for comparison with other parameter sets, we performed corresponding experiments on non-detached parts of the electrodes. However, their deposited platinum mass and specific surface area cannot be compared to the other parameter sets since these results are governed by the extent of fractures and layer delamination.

An increase in scan rate leads to a similar transition in surface texture from a cauliflower-like structure to a flat surface with mud-crack pattern as already observed for increasing copper content and decreasingly negative scan limits. Electrodes fabricated at 1 mV s^{-1} and 10 mV s^{-1} also show the crater-like features (see arrow-labels in Figure 4), which have already been observed for electrodes fabricated with a negative scan limit of -0.800 V vs. SCE (see Figure 3) and are attributed to the formation of hydrogen bubbles. On the nanoscale, the surface of the cauliflower-like spheres fabricated at the slow scan rate of 1 mV s^{-1} exhibits individual sharp-edged particles approximately 50 nm in diameter. At a scan rate of 10 mV s^{-1} these particles are approximately 100 nm in diameter and exhibit less sharp dendritic features.

Considering the roughness factors of the electrodes fabricated at scan rates of 1 mV s^{-1}, 10 mV s^{-1} and 50 mV s^{-1} a trend toward increasing specific surface is obtained for decreasing scan rates (see Table III). The longer deposition times per cycle which result from application of slower scan rates result in an enhanced precursor depletion enforcing a more dendritic structure growth compared to faster scan rates. Faster scan rates more often enable concentration relaxation during the non-deposition periods (E > 0.5 V vs. SCE) after comparably shorter deposition times (E < 0.5 V vs. SCE) and thus lead to a lower extent of precursor depletion during the deposition process (also see the discussion section). This increase in specific surface at lower scan rate is achieved at approximately the same deposited platinum mass. Consequently, a slightly higher surface percentage of platinum atoms is observed for electrodes fabricated at 1 mV s^{-1} and 10 mV s^{-1} compared to those fabricated at 50 mV s^{-1}.

EDX results show a tendency toward lower copper content in the bulk at faster scan rates (see Table III). This trend is also supported by the lattice constant calculated from XRD analysis, which are closer to that of pure platinum (3.92 Å) for faster scan rate.[35] This is assumed to be an effect of pure platinum deposition occurring in the potential range of 0.2 < E < 0.5 V vs. SCE in the anodic and cathodic scan consequent to the different redox-potentials of platinum and copper. At faster scan rates this coverage with platinum occurs more often but at a lower thickness compared to at slower scan rates. This leads to a better accessibility of the residual copper and thus to a facilitated dissolution of copper compared to at slower scan rates. Different to the bulk copper content analyzed by EDX, the surface-near copper content evaluated by XPS shows no significant changes in dependence of the

scan rate. Most probably the residual surface-near copper content of 4–6% which is typically observed for all tested samples corresponds to the physical limit of copper dissolution under the applied dealloying conditions (during fabrication and electrode characterization).[26,38]

Results and Discussion: Control of surface morphology

Parameter dependent effects on surface texture.— Deposition conditions requiring high mass transport rates and thus enforcing precursor depletion (more negative scan limit, slower scan rate and lower Cu^{2+} concentration) lead to cauliflower-like structures and sharp features on the nanoscale. The cauliflower-like morphology can be explained to be a consequence of interparticle diffusion coupling (IDC):[39] During deposition, precursor concentration is depleted in vicinity of each nucleation spot (depletion region). Overlapping depletion regions of neighboring particles lead to a decelerated growth of the corresponding particles compared to neighbor-free growth. Therefore increasingly broad size distributions result from IDC at high deposition rates or low precursor concentrations and finally agglomeration of neighboring particles result in the observed sphere-dominated structures. Different to this the comparably smooth top surface of the mud-crack patterns are obtained at lower deposition rates.

Parameter dependent effects on specific surface area.— Increasing specific surface area is obtained with increasing copper concentrations, more negative scan limit and slower scan rates. For increasing copper concentrations we attribute the increase in specific surface to an increasing copper content in the co-deposited alloy which enables a more effective dealloying process (also see percentage of surface platinum atoms in Table I). The application of increasingly negative scan limits corresponds to an expansion of the deposition time per deposition cycle. Hence, the increasing specific surface at increasingly negative scan limits is an effect of higher mass of platinum that is deposited during the extended deposition time (compare Table II). In case of scan rate variation we attribute the increase in specific surface observed for slower deposition times to precursor depletion during deposition due to the longer deposition times per cycle. During fast scans short deposition times are alternated with periods during which no deposition proceeds and thus concentration relaxation is obtained throughout major parts of the electrode surface. In contrast, the comparably long deposition periods (per cycle) at slow scan rates result in high precursor depletion and thus deposition occurs predominantly at the outer regions of the electrode, leading to the more dendritic structure[1,40] compared to with fast scan speeds.

Relationship between surface texture and specific surface.— No general correlation can be obtained when comparing specific surface area and surface texture (cauliflower-like or mud-crack pattern). With

increasingly negative scan limits and slower scan rates a larger specific surface area is obtained and the electrode morphology changes from an almost flat mud-crack pattern to the cauliflower-like structure. In contrast, an increase in Cu^{2+} concentration results in higher specific surface area and a transition from cauliflower-like structure to flat mud-crack pattern. Thus, high surface areas can be achieved at either high or low accessibility (controlled by surface texture). Both combinations are relevant for application: On the one hand, a high surface area at low accessibility would for instance be beneficial for the sensitivity of non-enzymatic glucose sensors operated in presence of interfering substances.[6–8] On the other hand, neuronal recording electrodes require a high surface and high mass transport (accessibility) for efficient signal transfer.[9,10]

Parameter dependent effects on structure composition.— Nanostructure analysis by XRD showed no significant differences in dependence of the fabrication parameters, except for the copper content. For all electrodes, nanocrystalline structures of the fcc type were observed from XRD analysis (see Figures S5). Additional superstructure reflection peaks indicating long range order or intermetallic phase formation as reported for the compositions $CuPt_7$ (12.5 at–% Cu,[35]) or $CuPt_3$ (25.0 at–% Cu,[41]) could not be observed. Thus the nanocrystals are made from mixed crystals with statistical distribution of platinum and copper. The average sizes of the crystallites within the different electrode structures were found to be in the range of 5 to 20 nm.

From EDX analysis the copper content in the bulk was shown to range from 10 to 21%, whereas XPS analysis revealed a significantly lower copper content near the surface of typically 4–6%. Such a core-shell composition of the electrode structures with a copper-rich core (bulk) and a copper-poor shell (surface) was observed for all tested electrodes. Therefore the existence of a core-shell structure can be regarded as a general property of electrodes fabricated by cyclic electrodeposition of PtCu alloy.[11]

Furthermore, EDX analysis indicates a trend toward decreasing residual copper with increasing scan rates. This observation is attributed to elongated periods during which only platinum is deposited und thus residual copper is embedded in the bulk.[11] This trend was attributed to different thicknesses of platinum coverage resulting from the different platinum deposition periods (0.2 < E < 0.5 V vs. SCE) per cycle when the scan rate is varied. In contrast, variations in negative scan limit and Cu^{2+} concentration showed no significant influences on the elemental composition. No influence was expected by variation of the negative scan limit, since this variation does not substantially influence the alloy composition, dealloying process or platinum coverage. Increasing Cu^{2+}-concentrations of course lead to a higher copper content in the alloy, but also a higher copper contents facilitate dealloying.[38,42,43] Therefore it is not astonishing, that no significant differences in the residual copper content were observed in dependence of the Cu^{2+}-concentration.

From XPS analysis a surface-near copper content of typically 4–6% is observed independent of the actual fabrication parameters. This indicates that the surface-near composition is related to a physical limit for copper dissolution under the chosen conditions for dealloying (here: CV scans for electrode cleaning, 10 cycles, 1.400 to −0.400 mV vs. SCE, 50 mV s^{-1}, 0.5 mol l^{-1} H_2SO_4). Such an incomplete dissolution of the less noble metal component during dealloying is also known from other dealloying experiments.[25,26,43,44] Retention of the less precious metal component is attributed to passivation of the atomic surface rearrangement during dealloying which can either be caused by a stable alloy formation, oxide layer, or surface-near depletion of the less precious component.[43,44]

The analysis of electronic states by XPS revealed platinum and most probably also copper to be present in zero-valent, metallic state. In case of copper, also a coexistence of Cu_2O is possible, since Cu^+ leads to the same binding energy of the $2p_{3/2}$ state as Cu^0 and thus cannot be distinguished from the metallic state from XPS spectra. Different to this, the presence of CuO can be excluded, since this would lead to a shift in binding energy and to shake-up satellites in the 2p signal which is not observed in any of the XPS spectra. This is supported by XRD analysis which neither showed Cu_2O nor CuO.

Conclusion

In conclusion, we demonstrated that cyclic electrodeposition of PtCu alloys is a versatile method for the fabrication of porous platinum structures not only with high specific surface area, but also with different surface textures ranging from cauliflower-like to almost flat mud-crack pattern structures. In this context, all investigated parameters - copper concentration, negative scan limit, and scan rate - have a significant effect on surface texture and specific surface area.

At deposition conditions at which strong precursor depletion occurs (low Cu^{2+} concentration, increasingly negative scan limit, slow scan rate), cauliflower-like surface textures are obtained. In principle, such structures possess a higher accessibility and thus higher mass transport rates compared to the mud-crack pattern morphologies. Therefore electrodes with cauliflower-like patterns are for instance beneficial for the use as stimulation electrodes.[9,10] Different to this, higher concentration of Cu^{2+}, less negative scan limits and higher scan rates lead to smoother surface textures (mud-crack pattern). Despite of the smooth surface texture, roughness factors of 1790 to 3740 were obtained for electrodes with mud crack patterns. Such electrodes, featuring a specific surface at low mass transport accessibility are good candidates for non-enzymatic glucose sensor or glucose fuel cell electrodes operated in presence of interfering substances.[6–8]

At high concentrations of Cu^{2+} (100 mmol l^{-1}), more negative scan limits (−0.800 V vs. SCE) and slow scan rates (1 mV s^{-1}) roughness factors of 3740 ± 270, 3790 ± 370 and 3930 ± 370 were observed. Thus, these parameter changes enable an enlargement in specific surface area of approximately 30% compared to electrode fabrication with standard parameters (roughness factor 3040 ± 300).[11] Since high amounts of platinum (10–20 mg per cm^2 electrode footprint) are required to achieve these high roughness factors this fabrication method is not well suited to large scale applications. Nevertheless, this process is of high relevance to special applications such as neurostimulation, implantable fuel cells, and non-enzymatic electrochemical sensors. Such systems benefit from highly rough electrodes that can be precisely fabricated by a facile electrodeposition process, and compared to the overall functionality of these devices material costs are less relevant.

None of the investigated parameters enabled the complete removal of copper from the electrode structures, since copper gets buried during periods in which only platinum is deposited on top of the co-deposit.[11] However, our results suggest that the exposed surface of the electrodes is platinum rich (>90% platinum content). Furthermore, cyclic voltammetry experiments revealed stable electrode surfaces, in particular no oxidation peaks attributable to copper dissolution appeared. Nevertheless, for biomedical application of the presented electrodes (e.g. neuroprostheses or implantable glucose fuel cells) dedicated biocompatibility and copper-leaching studies will be required.

Associated content – supplementary material.— Five additional figures are online providing further figures analyzing the deposition process in dependence of different copper concentrations (Figure S1 and S2) and the data of XPS (Figure S3–S5) and XRD analysis (Figure S6).

References

1. A. Kloke, F. von Stetten, R. Zengerle, and S. Kerzenmacher, *Adv. Mater.*, **23**, 4976 (2011).
2. A. C. Chen and P. Holt-Hindle, *Chem. Rev.*, **110**, 3767 (2010).

3. W. Vielstich, A. Lamm, and H. A. Gasteiger, *Handbook of Fuel Cells; Volume 1: Fundamentals and Survey of Systems*, pp. 143–433 John Wiley & Sons, Chichester (2003).
4. K. M. Bratlie, H. Lee, K. Komvopoulos, P. D. Yang, and G. A. Somorjai, *Nano Lett.*, **7**, 3097 (2007).
5. G. A. Somorjai and Y. M. Li, *Top. Catal.*, **53**, 832 (2010).
6. Y. Y. Song, D. Zhang, W. Gao, and X. H. Xia, *Chem. Eur. J.*, **11**, 2177 (2005).
7. S. Park, T. D. Chung, and H. C. Kim, *Anal. Chem.*, **75**, 3046 (2003).
8. J. H. Yuan, K. Wang, and X. H. Xia, *Adv. Funct. Mater.*, **15**, 803 (2005).
9. S. Mailley, M. Hyland, P. Mailley, J. A. McLaughlin, and E. T. McAdams, *Bioelectrochem.*, **63**, 359 (2004).
10. K. C. Cheung, *Biomed. Microdevices*, **9**, 923 (2007).
11. A. Kloke, C. Köhler, R. Zengerle, and S. Kerzenmacher, *Adv. Mater.*, **24**, 2916 (2012).
12. S. W. Lee, S. Chen, J. Suntivich, K. Sasaki, R. R. Adzic, and Y. Shao-Horn, *J. Phys. Chem. Lett.*, **1**, 1316 (2010).
13. M. T. Koper, *Nanoscale*, **3**, 2054 (2011).
14. Z. Quan, Y. Wang, and J. Fang, *Acc. Chem. Res.*, (2012).
15. N. Tian, Z. Y. Zhou, S. G. Sun, Y. Ding, and Z. L. Wang, *Science*, **316**, 732 (2007).
16. S. Trasatti and O. A. Petrii, *J. Electroanal. Chem.*, **327**, 353 (1992).
17. B. D. Cullity and S. R. Stock, *Elements of X-Ray Diffraction*, 3rd edition, Prentice-Hall Inc. (2001).
18. A. Altomare and G. Giacovazzo, in *Powder Diffraction: Theory and Practice*, 1st ed., pp. 211–212, R. E. Dinnebier and S. J. L. Billinge, RSC Publishing, Cambridge (2008).
19. P. Scardi, in *Powder Diffraction: Theory and Practice*, 1st ed., R. E. Dinnebier and S. J. L. Billinge, pp. 379–381, RSC Publishing, Cambridge (2008).
20. R. Jenkins and R. L. Snyder, in *Introduction to X-Ray Powder Diffractometry*, 1st ed., pp. 89–91, John Wiley & Sons, New York (1996).
21. C. L. Green and A. Kucernak, *J. Phys. Chem. B*, **106**, 1036 (2002).
22. J. J. Mallett, E. B. Svedberg, S. Sayan, A. J. Shapiro, L. Wielunski, T. E. Madey, P. J. Chen, W. F. Egelhoff, and T. P. Moffat, *Electrochemical and Solid-State Letters*, **8**, C15 (2005).
23. H. T. Liu, P. He, Z. Y. Li, and J. H. Li, *Nanotechnol.*, **17**, 2167 (2006).
24. K. S. Choi, E. W. McFarland, and G. D. Stucky, *Adv. Mater.*, **15**, 2018 (2003).
25. P. Strasser, S. Koh, and J. Greeley, *Phys. Chem. Chem. Phys.*, **10**, 3670 (2008).
26. S. Koh and P. Strasser, *J. Amer. Chem. Soc.*, **129**, 12624 (2007).
27. P. Strasser, *Reviews in Chemical Engineering*, **25**, 255 (2009).
28. J. F. Moulder, W. F. Stickle, P. E. Sobol, and K. D. Bomben, *Handbook of X Ray Photoelectron Spectroscopy: A Reference Book of Standard Spectra for Identification and Interpretation of XPS Data*, pp. 86–87 and pp. 180–181, Physical Electronics Division, Perkin-Elmer Corp., Eden Prairie MN (1995).
29. A. S. Arico, A. K. Shukla, H. Kim, S. Park, M. Min, and V. Antonucci, *Appl. Surf. Sci.*, **172**, 33 (2001).
30. J. S. Hammond and N. Winograd, *J. Electroanal. Chem.*, **78**, 55 (1977).
31. J. S. Lee and W. Y. Choi, *J. Phys. Chem. B*, **109**, 7399 (2005).
32. J. B. Reitz and E. I. Solomon, *J. Amer. Chem. Soc.*, **120**, 11467 (1998).
33. S. Larsson, *Chem. Phys. Lett.*, **40**, 362 (1976).
34. J. P. Espinos, J. Morales, A. Barranco, A. Caballero, J. P. Holgado, and A. R. Gonzalez-Elipe, *J. Phys. Chem. B*, **106**, 6921 (2002).
35. A. Schneider and U. Esch, *Zeitschrift für Elektrochemie und angewandte physikalische Chemie*, **50**, 290 (1944).
36. L. Vegard, *Zeitschrift für Physik A Hadrons and Nuclei*, **5**, 17 (1921).
37. A. Ott, L. A. Jones, and S. K. Bhargava, *Electrochem. Commun.*, **13**, 1248 (2011).
38. D. V. Pugh, A. Dursun, and S. G. Corcoran, *J. Electrochem. Soc.*, **152**, B455 (2005).
39. R. M. Penner, *J. Phys. Chem. B*, **106**, 3339 (2002).
40. H. S. Kim, N. P. Subramanian, and B. N. Popov, *J. Power Sources*, **138**, 14 (2004).
41. Y. C. Tang, *Acta Crystallogr.*, **4**, 377 (1951).
42. J. Erlebacher, M. J. Aziz, A. Karma, N. Dimitrov, and K. Sieradzki, *Nature*, **410**, 450 (2001).
43. J. Erlebacher, *J. Electrochem. Soc.*, **151**, C614 (2004).
44. Y. Liu, S. Bliznakov, and N. Dimitrov, *J. Electrochem. Soc.*, **157**, K168 (2010).